Probing quasigeostrophic turbulence via complex networks

V. R. Krishna Priya ,[1,*] Snehal Sunil Patil ,[2] Somnath Roy ,[2]
Konduri Aditya ,[3] and Rajaram Lakkaraju [2,†]
[1]*Centre for Computational and Data Sciences, Indian Institute of Technology Kharagpur, West Bengal-721302, India*
[2]*TuRbulent Interfaces And Dispersion (TRIAD), Department of Mechanical Engineering, Indian Institute of Technology Kharagpur, West Bengal-721302, India*
[3]*Department of Computational and Data Sciences, Indian Institute of Science, Bangalore-560012, India*

(Received 3 October 2024; accepted 18 April 2025; published 5 May 2025)

Using statistical analysis and complex networks, we study the role of inverse Rossby deformation radius, λ, on freely decaying quasi-geostrophic turbulence dynamics. We find that the area fraction occupied by vortices remains constant over an extended duration for all values of λ. We establish an energy spectrum scaling based on a self-similar distribution of vortices of area A during this period. Our findings suggest that the vortex number density follows the relationship $n(A) \sim N_v A^{-p}$, and the inertial range energy spectra scales as k^{-7+2p}, where N_v represents the number of vortices and p depends on λ. To investigate vortical interactions, we construct a spatiotemporal weighted network. Our analysis uncovers two distinct strength distributions: (1) a briefly observed scale-free distribution resulting from nonlocal interactions when $\lambda \ll k_0$, and (2) a truncated scale-free distribution due to local interactions over an extended period when $\lambda \gg k_0$, where k_0 denotes the initial characteristic wave number at which the total energy is at its maximum. Both networks are robust against random disturbances but are vulnerable to targeted attacks on their hubs. Additionally, we found that these network hubs contribute to the large-scale energy spectra, which can be reconstructed using only 1% of the total degrees of freedom in a quasi-geostrophic turbulent field.

DOI: 10.1103/PhysRevFluids.10.054402

I. INTRODUCTION

Oceanic eddies are swirling bodies of water ubiquitous in the global oceans, typically having spatial scales ranging from tens to hundreds of kilometers and temporal scales of days to months [1,2]. These eddies play an indispensable role in the long-term dynamics of general ocean circulation [3,4], biogeochemical systems [5], including marine life and plankton [6–8], and the climate of our planet [9]. It is now universally recognized that oceanic eddies are instrumental in transporting heat from tropical regions to the poles [10], although this effect can vary by region. For instance, mesoscale eddy heat transport is dominant in the Southern Ocean and the Kuroshio Current [11,12]. Additionally, these eddies play a vital role in transferring gases and tracers from the Southern Ocean mixed layer into the upper 2000 m of ocean interior [13] and are fundamental in establishing horizontal and vertical stratification in the Southern Ocean [14]. Oceanic eddies exhibit a wide range of horizontal scales influenced by latitude. Near the equator at approximately 5 °S, the radius of these eddies is around 200 km, shrinking to about 75 km in midlatitudes at 60° and about 6 km in

*Contact author: krishnapriya.vr0@gmail.com
†Contact author: rajaram.lv@gmail.com

high latitudes [2,15]. The size of eddies is crucial in determining how strongly they interact with the atmosphere. For instance, the strength of this coupling decreases from the equator toward the poles as eddy size decreases in that direction [16]. Recent studies also indicate that larger eddies (>50 km) have a more significant and deeper imprints on tracer distributions, as well as a stronger influence on heat and CO_2 fluxes between the atmosphere and the South-East Atlantic Ocean, compared to smaller eddies (<50 km) [17]. The typical movement speed of eddies averages about 1 km per hour [18], with wide variations in their lifespans. Recent studies confirm that oceanic eddies can exist for up to a year in the subtropical westward flows (between 30° to 60° in both hemispheres), as well as in the subtropical South Indian Ocean (at 20 °S–30 °S) and the Northeast Atlantic Ocean (at 36 °N–90 °N) [19]. Regardless of the spatial and temporal scales, eddies consistently exchange salt and nutrients while showcasing short- and long-range interactions with the main currents [20]. The interactions of these powerful eddies are crucial for decision-making regarding existing and future offshore oil drilling operations [21], as they account for nearly 50% of the energy present in ocean circulation [22]. The eddy genesis and termination processes occur frequently during interactions [23], facilitating energy exchange between eddies and the broader ocean circulation system. The dynamics of these eddies are predominantly governed by gravity and planetary rotation [24], though other significant factors are also at play. The Rossby radius of deformation (or the inverse of the Rossby deformation wave number, λ) delineates whether gravity or planetary rotation is the dominant force in stabilizing flow dynamics near the surface. Specifically, when λ is very large, planetary rotation dictates the dynamics to maintain free surface height anomalies, while a reversal indicates relative tendencies of gravity to relax the free surface. On average, the Rossby deformation radius is approximately 240 km near the equator, dropping to less than 10 km at higher latitudes [25].

Under the influence of rotation and density stratification, the intricate nonlinear interactions among eddies (or more popularly, the vortices) can be effectively understood through the lens of minimalistic fluid dynamics, specifically by employing the two-dimensional (2D) quasi-geostrophic (QG) turbulent flow framework [26]. This perspective is not just theoretical; it unveils the fascinating formation of jets and a broad spectrum of vortex populations [27,28]. In purely 2D turbulence simulations ($\lambda = 0$), where rotational effects are deemed insignificant [29], large-scale organized vortices arise from carefully selected initial random flow fields, catalyzed by the dual effects of the inverse energy cascade and the direct enstrophy cascade [26]. Moreover, these vortices do not merely coexist; they dynamically merge and grow over time. Their average radius ($\bar{r}$) expands with time (t) following a power law, $t^{\xi/4}$, while the number density of these vortices diminishes as $t^{-\xi}$, where $\xi \approx 0.75$ [30]. The long-range interactions between these vortices, where distant ones can influence each other despite intervening vortices, occur through the logarithmic Green's function. This results in stable filamentary flow structures that roll up in the absence of vortices, significantly impacting the overall energy transfer mechanisms [31,32]. While the emergence of substantial coherent vortices may contribute to intermittency in 2D turbulence [33], we also see that the energy spectrum in terms of wave number (k) adheres to $\mathcal{E}(k) \sim k^{-\alpha}$ in the inertial range, with a spectral exponent satisfying $3 < \alpha \leqslant 5$ [26,34,35]. This important detail showcases that the exponent is notably steeper than 3, diverging from the predictions made by Batchelor and Kraichnan's theories in the absence of coherent vortices [36,37]. When considering initial flow fields that meet specific Gaussian statistical conditions, the energy spectrum in the small wave numbers shows $\mathcal{E}(k) \sim Jk^{-1} + Lk + Ik^3 + \mathcal{O}(k^5)$, where J is a function of two-point vorticity correlation, L represents the Saffman integral, and I denotes the Loitsyansky integral [32]. Paralleling other crucial invariants in the inertial range, like energy and enstrophy, both J and L also act as invariants in the small wave number regime. Depending on initial conditions, the energy spectrum may conform to Jk^{-1}, Lk, or Ik^3 [38].

In geophysical turbulence, we often encounter $\lambda \neq 0$. For length scales larger than λ^{-1}, quasi-frozen vortices develop, which evolve slowly over time. In this case, stream function dominates potential vorticity, and the QG equation reduces to the advection of stream function by relative vorticity on rescaled times proportional to λ^{-2}. Importantly, vortices exceeding the deformation radius (or λ^{-1}) resist merging, thereby preventing the transfer of energy to larger scales. Nevertheless, recent numerical studies [39,40] have revealed that vorticity fronts comparable to $\mathcal{O}(\lambda^{-1})$ can facilitate potential energy transfer, thereby obstructing the formation of quasi-frozen vortices. In the large λ limit, the energy spectrum in the inertial range adheres to $\mathcal{E}(k) \sim k^{-6}$, whereas for small wave numbers, the spectrum evolves to $\mathcal{E}(k) \sim \lambda^2(Lk^{-1} + Ik + Mk^3) + Lk + Ik^3 + \mathcal{O}(k^5)$, where M and I serve as invariants linked to two-point vorticity correlation functions. Furthermore, the evolution of flow from a selected narrow banded initial energy spectra gives $\mathcal{E}(k) \sim k^4$ within the small wave number range [41].

While previous research has extensively studied both the small and large Rossby deformation wave number regimes ($\lambda = 0$ and $\lambda \gg 1$), there remains a significant gap in our understanding of the intermediate λ range. This gap hinders our grasp of spatiotemporal patterns, vortex merging and breakup processes, and essential statistics like size distribution, spectral scalings, area packing fraction, and interaction quantification. A robust vortex population model that elucidates the energy transfer mechanism and its dependency on λ, particularly regarding the number of vortices and their spatial occupation within a given domain, is yet to be proposed. To address these knowledge gaps, we conducted targeted QG-decaying turbulence simulations in biperiodic, square domains across a broad range of λ. Our analysis enabled us to quantify vortex populations and their interactions, revealing local and nonlocal interactions via advanced complex network techniques. Recent explorations [42–48] underscored the importance of graph-theory-based methods to study complex fluid dynamical systems, where nodes symbolize system constituents (e.g., vorticity), links represent vortical interactions, and link weights correspond to interaction strength. The total sum of link weights at any node reflects its overall strength [45]. Observations indicate that node strength distributions often exhibit scale invariance as a power law, characterized by negative scaling exponents ranging from 2 to 3 [49]. The underlying dynamics of these scale-invariant networks can be elucidated through growth and preferential attachment frameworks [50], allowing us to identify critical nodes within a turbulent system. This approach enables a low-dimensional representation of the system, distilling complex interactions into only a few hundred pivotal nodes to better capture the behavior of systems with millions of degrees of freedom.

In our QG studies, we emphasize the vital contribution of vortices to turbulence dynamics. We have meticulously identified critical vortices that influence short- and long-range interactions. Our findings demonstrate that the construction of a vortical network not only provides valuable metrics for assessing interaction strength and range but also enhances our understanding of energy spectra scaling, transcending the limitations of traditional statistics-based models. This research opens avenues for analyzing and predicting turbulent behavior in complex systems.

Section II is for numerical details, Sec. III for flow features, vortex identification, and scaling, Sec. IV is for network-analysis-based vortex strength quantification, and in Sec. V we have provided the summary and conclusions with future scope.

II. NUMERICAL DETAILS

The quasi-geostrophic equation that describes the dynamics of a rapidly rotating fluid layer with a deformable free surface [24] in terms of the potential vorticity (q) and stream function (ψ) is given by

$$q_t + \mathcal{J}(\psi, q) = -\nu \nabla^4 q, \tag{1}$$

where $q = (\Delta - \lambda^2)\psi$, Δ is the two-dimensional (2D) Laplacian, ν is the hyperviscosity, $\mathcal{J}(\psi, q) = \partial_x\psi\partial_y q - \partial_y\psi\partial_x q$ is the Jacobian, the subscripts x and y represent the partial spatial derivatives, and t represents the partial time derivative. The Rossby deformation wave number (or the inverse of the Rossby radius of deformation), $\lambda = f/\sqrt{gH}$, plays an important role in geophysical turbulence for a given Coriolis parameter (f), the acceleration due to gravity (g), and the ocean layer mean depth (H). The inviscid quadratic invariants of Eq. (1) are the total energy $E = \langle -\psi q\rangle/2$ and the potential enstrophy $Q = \langle q\Delta\psi\rangle/2$, where $\langle\cdot\rangle$ is the spatial average over

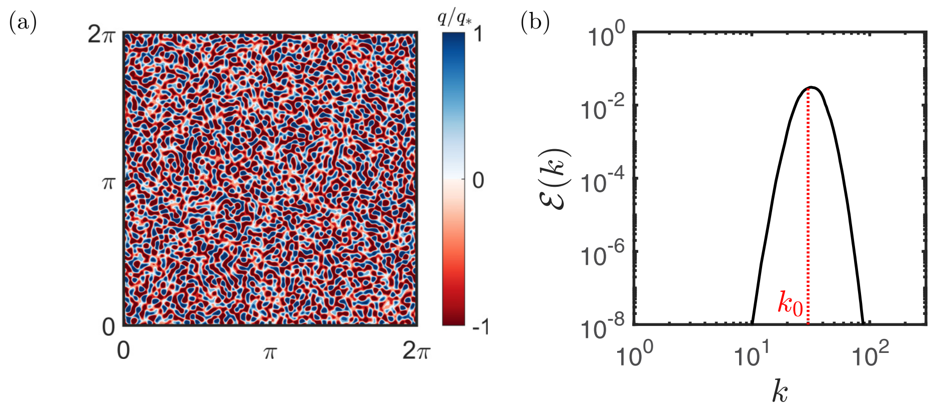

FIG. 1. Initial condition for simulations: (a) Potential vorticity (q) on $[0, 2\pi] \times [0, 2\pi]$ computational domain. q_* is the rms value and serves as a scale. Colorbar ranges from -1 (red) to 1 (blue). (b) Initial energy spectrum $\mathcal{E}$ vs wave number k. Spectrum is peaked at $k_0 = 30$ (dashed line).

the domain. The total energy, $E = \langle|\nabla\psi|^2\rangle/2 + \lambda^2\langle\psi^2\rangle/2$, consists of the kinetic energy and the potential energy. The inviscid dynamics also conserve an infinite class of other integral quantities known as the Casimirs [32].

We perform direct numerical simulations of a doubly periodic square box of size $2\pi \times 2\pi$ by integrating Eq. (1) using the GeophysicalFlows.jl pseudospectral techniques [51] with a 2/3 rule for dealiasing and fourth-order Runge-Kutta method in time. We used a spatial resolution of 2048×2048 (see grid independence study in Supplemental Material [52]) with a hyperviscosity $\nu = 5 \times 10^{-9}$ to preferentially dampen the potential enstrophy at small scales, leaving more energetic scales nearly inviscid. The initial vorticity field is created by generating uniform random numbers ranging from 0 to 2π for the phase of each Fourier component of the stream function, similar to Refs. [41,53]. Such initialization corresponds to the single-point probability distribution of the initial vorticity field as Gaussian so that the emergence of large-scale coherent vortices and their interaction, in the long run, can be studied [28,41,44,54]. The initial energy spectrum consists of a narrow band in the form $\mathcal{E}(k) = Ck^{30}/(k + k_0)^{60}$, with characteristic wave number $k_0 = 30$, and the proportionality constant C is chosen so that initial kinetic energy as 0.5, with the Reynolds number based on the initial conditions as $\mathcal{O}(10^4)$. The normalized initial potential vorticity field (q/q_*) and the total energy spectrum for the chosen initial conditions are shown in Fig. 1. The subscript $*$ denotes the root mean square of a quantity. Our results are shown in normalized time for which the eddy turnover time $\tau_0 = (1 + [\lambda E/(\int_0^\infty k\mathcal{E}(k)dk)]^2)/\sqrt{\langle|\nabla\psi|^2\rangle}$, constructed based on initial conditions. When $\lambda = 0$, this definition is equivalent to that commonly used in 2D turbulence studies [26], which are typically carried out until $t = 1000\tau_0$. For higher λ, simulations are carried out until $t = 1500\tau_0 - 2000\tau_0$, similar to Ref. [55]. In this paper we studied QG turbulence for λ ranging from 0 (a pure 2D turbulence) to 100 (large-scale QG turbulence). Table I shows the complete list of simulations for which the initial field is the same irrespective of λ. Additional validation studies of our work are mentioned in the Supplemental Material [52].

III. FLOW FEATURES AND ENERGY SPECTRUM IN QG TURBULENCE

The potential vorticity (q) transitions from an initial Gaussian distribution to discrete and isolated vorticity concentrations, known as coherent vortices, persist far longer than the typical eddy turnover time through mutual advection and vortex merging mechanisms. For $\lambda = 0$, we observe broadly distributed vortices alongside intricate filamentary structures, as illustrated in Fig. 2(a), and animation A1 is provided in the Supplemental Material [52]. However, as λ increases (notably,

TABLE I. Simulations and parameters used in our work. Columns are: (1) Rossby deformation wave number (λ), (2) initial eddy turnover time (τ_0), and (3) end simulation time ($t_{\max}$ in τ_0 units). Based on initial conditions, (4) for kinetic energy ($K = \langle|\nabla\psi|^2\rangle/2$), (5) for potential energy ($P = \lambda^2\langle\psi^2\rangle/2$), (6) for total energy ($E = K + P$), and (7) for total number of vortices (N_v). Note that the initial kinetic energy is the same for all simulations.

λ	τ_0	$t_{\max}$ (in τ_0)	Kinetic energy $K = \frac{1}{2}\langle\lvert\nabla\psi\rvert^2\rangle$	Potential energy $P = \frac{1}{2}\lambda^2\langle\psi^2\rangle$	Total energy $E = K + P$	$N_v(0)$
0	0.0303	1000	0.5	0	0.5	1704
1	0.0303	1000	0.5	0.000527	0.5005	1704
5	0.0317	1000	0.5	0.0132	0.5132	1704
10	0.0332	1000	0.5	0.0528	0.5528	1704
20	0.0422	1000	0.5	0.2111	0.7111	1704
30	0.0579	1500	0.5	0.4750	0.9750	1704
40	0.0805	1500	0.5	0.8444	1.3444	1704
50	0.1098	2000	0.5	1.3194	1.8194	1704
60	0.1459	2000	0.5	1.9000	2.4000	1704
70	0.1888	2000	0.5	2.5861	3.0861	1704
80	0.2383	2000	0.5	3.3778	3.8778	1704
90	0.2945	2000	0.5	4.2750	4.7750	1704
100	0.3573	2000	0.5	5.2778	5.7778	1704

for $\lambda \geqslant 10$), we observe a collection vorticity monopoles, characterized by a decrease in q as one moves away from the vortex center. These vortices can be either separate or partially joined with neighboring vortices of the same sign, as shown in Fig. 2(b), and animation A2 is provided in the Supplemental Material [52]. Further increasing λ (up to 50) leads to reduced separation among vortices [depicted in Fig. 2(c)], and animation A3 is provided in the Supplemental Material [52], resulting in being nearly stationary, establishing a quasi-steady state for an extended period. A quantitative analysis of the number, radius, and closeness of vortices using a packing fraction is studied in the following section.

Figures 2(d)–2(f) depict the total energy spectra $\mathcal{E}(k)$ and potential enstrophy spectra $\mathcal{Q}(k)$ at different time intervals. In the inertial range, the energy spectra for $\lambda = 0$ show a scaling of $\mathcal{E}(k) \sim k^{-4}$, while the enstrophy spectra scale as $\mathcal{Q}(k) \sim k^{-2}$, echoing results from Ref. [56]. Our energy spectra are steeper than the traditional k^{-3} observed in Refs. [36,37]. Over time, the $\mathcal{E}(k)$ peak shifts towards smaller wave numbers, illustrating an inverse energy cascade. With increased λ, the energy spectra steepen further, revealing $k^{-5.2}$ for $\lambda = 10$ and $k^{-5.8}$ for $\lambda = 50$. The energy spectra for $\lambda = 50$ also display time self-similarity, which is a notable deviation from $\lambda = 0$. Our findings on potential enstrophy spectra follow the relation $\mathcal{Q}(k) \equiv k^2\mathcal{E}(k)$. In the insets of these figures, time evolution of the total energy $E(= \int_0^\infty \mathcal{E}(k)dk)$ and potential enstrophy $Q(= \int_0^\infty \mathcal{Q}(k)dk)$ are shown for the different λ values. The total energy remains almost conserved, while potential enstrophy decays more rapidly due to finite Reynolds number effects. After an initial transient state, we observe a decay of $Q(t) \sim t^{-0.72}$, consistent with Ref. [57] and contrasting with the t^{-2} prediction from Ref. [37]. As λ increases, we observed $Q(t) \sim t^{-0.58}$ for $\lambda = 10$ and $t^{-0.5}$ for $\lambda = 50$.

The instantaneous probability density function (PDF) of potential vorticity $P(q/q_*)$ is shown in Fig. 3(a). For $\lambda = 0$, the PDFs transition from an initial Gaussian form into a stretched exponential distribution over time, characterized by wider tails (for $q > 6q_*$). As λ increases, these tails narrow, and for $\lambda \geqslant 30(\equiv k_0)$, the PDFs converge to a Gaussian-like distribution. To quantify deviations from Gaussianity, we calculate the normalized third moment (skewness) $S = \langle(q/q_*)^3\rangle/\langle(q/q_*)^2\rangle^{3/2}$ and the normalized fourth moment (flatness) $F = \langle(q/q_*)^4\rangle/\langle(q/q_*)^2\rangle^2$, as shown in Fig. 3(b). Across all λ, the third moment remains approximately zero ($S \approx 0$) due to symmetry in the PDF shape. For $\lambda = 0$, initial flatness F, which starts at 3, corresponding to a Gaussian distribution, rises

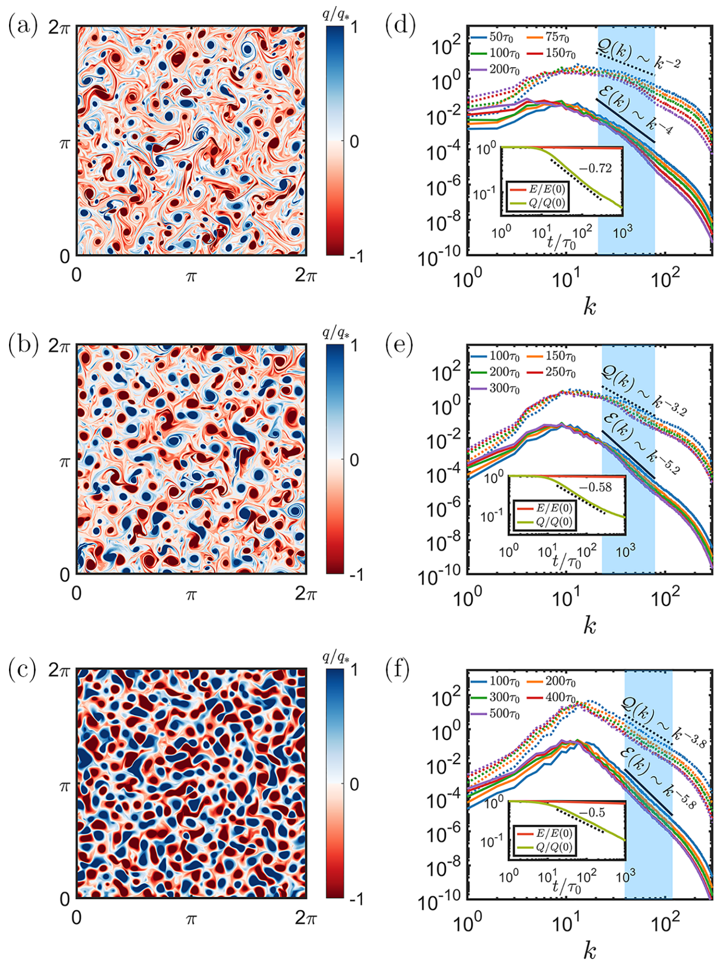

FIG. 2. Instantaneous normalized potential vorticity (q/q_*) at $t = 200\tau_0$ for (a) $\lambda = 0$, (b) $\lambda = 10$, and (c) $\lambda = 50$. Animations (A1, A2, A3) are provided in the Supplemental Material [52]. Total energy spectra, $\mathcal{E}(k)$, in continuous lines and potential enstrophy spectra, $Q(k)$, in dotted lines for (d) $\lambda = 0$, (e) $\lambda = 10$, and (f) $\lambda = 50$. Spectra nature is shown in the inertial range (blue shade). Insets in (d)–(f) show normalized total energy (E) and potential enstrophy (Q) as functions of time for respective λ. E conserves but Q decreases with time as $t^{-0.72\pm0.01}$ for $\lambda = 0$, $t^{-0.58\pm0.01}$ for $\lambda = 10$, and $t^{-0.5\pm0.01}$ for $\lambda = 50$.

with time to $F > 6$, which corresponds to stretched exponential distributions, aligning with results from Ref. [33]. For $\lambda \geqslant k_0(\equiv 30)$, the PDFs become leptokurtic, displaying flatness between 3 and 6. The exponential tails in vorticity for $\lambda < k_0$ imply a level of intermittency that could be due to the formation of coherent vortices. While we identify slowly evolving quasi-frozen vortices for $\lambda \geqslant k_0$, the PDFs do not display the anticipated broader tails in vorticity, underscoring the necessity for a deeper understanding of the statistical characteristics of the vortices and their interactions to decipher the QG energy spectra within the inertial range.

A. Vortex identification and population-based scaling of energy spectra

The quest for a universally accepted definition of a vortex remains ongoing [58], with multiple potential characterizations proposed. One claim is that "a vortex exists when instantaneous streamlines mapped onto a plane normal to the vortex core exhibit a roughly circular or spiral pattern

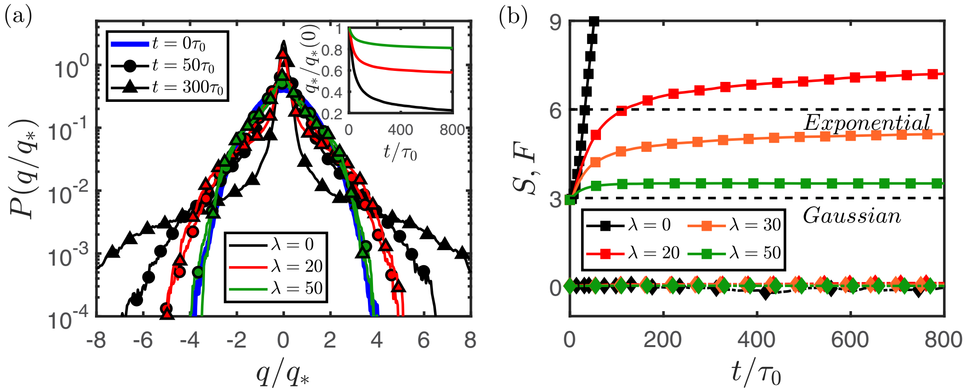

FIG. 3. (a) Probability density functions of single-point potential vorticity, $P(q/q_*)$, at $t = 50\tau_0$ (circles) and $300\tau_0$ (triangles). Blue line for initial state (which is a Gaussian distribution). Inset shows normalized rms potential vorticity (q_*) vs time (t). (b) Skewness (S) in diamonds and flatness (F) in squares as a function of time. Colors are black ($\lambda = 0$), red ($\lambda = 20$), orange ($\lambda = 30$), and green ($\lambda = 50$). With time, the PDF evolves from Gaussian ($F \approx 3$) to stretched exponential distribution ($F > 6$) for $\lambda < k_0(\equiv 30)$ and leptokurtic distribution ($F > 3$) for $\lambda \geqslant k_0$.

when viewed from a reference frame moving with the center of the vortex core" [59]. Alternatively, it can be identified as a space containing a positive second invariant of the velocity gradient tensor alongside low pressure, known as the $\mathbb{Q}$ criterion [60]. Other criteria include the second largest eigenvalue of the velocity gradient tensor (λ_2 criterion) [61] and the imaginary part of the complex eigenvalue pair of the velocity gradient tensor (the swirling strength criterion) [62]. Moreover, Vortex census [29] identifies vortices using a closed boundary encompassing approximately 80% of every extremum of $|q|$. Recent research [63–65] has emphasized the significance of the Rortex field, defined as $R = q - \sqrt{q^2 - 4\eta^2}$. In this context, a vortex is a connected region with $R \neq 0$, the vortex center is where $|R|$ reaches its maximum, and the vortex radius is given by $r_i = \sqrt{N_c \Delta x \Delta y/\pi}$. Here, η represents the imaginary part of the eigenvalues of the velocity gradient tensor, N_c counts the computational meshes satisfying the vortex definition, and Δx and Δy are the mesh size (or resolution). More details on the R field and identification of vortices are given in the Supplemental Material [52].

From the animations in the Supplemental Material [52], it is clear that the size of the vortices grows over time, accompanied by the emergence of small-scale filamentary structures. To accurately quantify the fraction of area occupied by the vortices in our setup—particularly during periods when a broader inertial range is observed—we have computed the packing fraction of vortices, $\Phi = (\sum_i^{N_v} \pi r_i^2)/(2\pi)^2$. Here N_v is the number of vortices, and r_i is the radius of ith vortex, and $(2\pi)^2$ is the area of the domain. As illustrated in Fig. 4(a), it is evident that Φ is mainly independent of time. This emphasizes that, over an extended duration, a state of balance is achieved between vortex advection and viscous dissipation. Our simulations reveal that time-averaged packing fraction (or $\langle\Phi\rangle_t$) increases with λ to each $\langle\Phi\rangle_t \approx 0.035$ for large $\lambda > 2k_0$. Figure 4(b) presents the number of vortices N_v and the average radius $\overline{r} = (\sum_i^{N_v} r_i)/N_v$ as a function of time. Our findings demonstrate that N_v decays as $t^{-\xi}$, while growth of $\overline{r}$ follows the relation t^{ζ}. Notably, for $\lambda = 0$ we find $\xi \approx 0.72$, similar to Ref. [66] and $\zeta \approx 0.38$. As λ increases, these exponents stabilize at $\xi \approx 0.44$ and $\zeta \approx 0.18$. The scaling exponents as a function of λ are shown in the inset.

Based on such stark contrast in the generated vortex populations, we propose a theory that accounts for area and number density and serves as a framework for understanding inertial range energy spectra. Imagine the identified population of vortices has a vortex number density $n(A)$ as a function of area A. The potential enstrophy Q_v and total energy E_v contained within these vortices

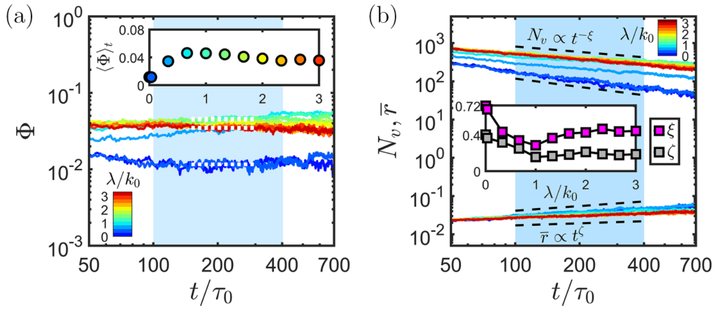

FIG. 4. (a) Packing fraction Φ as a function of time for different λ. Time-averaged packing fraction over the blue shaded region, ($\langle\Phi\rangle_t$), as a function of λ is shown in the inset. The dotted white line in the main figure corresponds to the constant $\langle\Phi\rangle_t$ for each λ. (b) Number of vortices (N_v) and mean radius ($\bar{r}$) as a function of time for different λ. The measured scaling exponents ξ and ζ for N_v and $\bar{r}$, respectively, as functions of λ are shown in the inset. Shaded region corresponds to the wider inertial range during $100\tau_0 < t < 400\tau_0$.

are defined similar to Ref. [67] as

$$Q_v = \frac{1}{2A_s}\int_0^{A_s} q_v \Delta\psi_v A n(A) dA, \quad \text{and} \quad E_v = \frac{1}{2A_s}\int_0^{A_s} q_v \psi_v n(A) dA,$$

where q_v and ψ_v represent the potential vorticity and the stream function, both assessed within the vortex, respectively, and A_s denotes an arbitrary domain size. It is important to note that the total enstrophy Q across the entire domain is formulated as $Q = \int_0^\infty \mathcal{Q}(k)dk \equiv \int_0^\infty k^2\mathcal{E}(k)dk$. Significantly, most energy in the flow field is associated with the vortices, allowing us to assert that $E \approx E_v$ (refer to Supplemental Material [52]).

By utilizing the R field, we estimate that the potential enstrophy $q_v\Delta\psi_v$ remains remarkably consistent, regardless of the vortex area A (as depicted in Fig. 5, where the time average of $q_v\Delta\psi_v$ deviates by less than 0.5 order over 2 orders of change in A). Employing the relation $A \sim k^{-2}$, which leads to $dA \sim k^{-3}dk$, allows us to derive

$$\mathcal{E}(k) \sim q_v\, \Delta\psi_v\, A_s^{-1}\, n(A)\, k^{-7}.$$

If the scaling of $n(A)$ follows A^{-p}, we find $\mathcal{E}(k) \sim k^{-7+2p}$. The time-averaged number density $n(A)$ for different λ is illustrated in Fig. 5. We observe that $n(A) \sim N_v A^{-1.5\pm0.1}$ for $\lambda = 0$, suggesting an energy spectrum proportional to $\sim k^{-4}$, aligning remarkably with our simulation findings [see

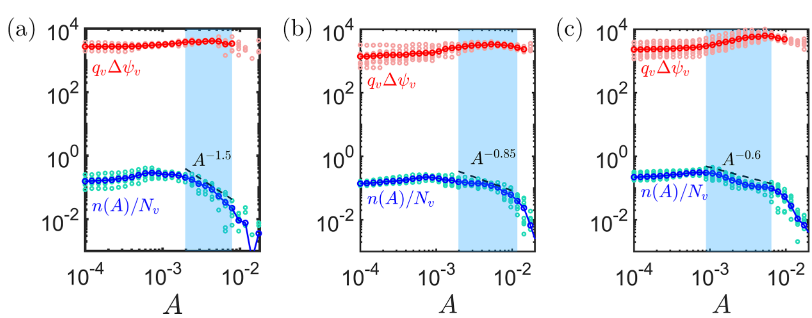

FIG. 5. Vortex statistics. Potential enstrophy in vortices ($q_v\Delta\psi_v$) as red circles and number densities ($n(A)/N_v$) as blue circles for (a) $\lambda = 0$, (b) $\lambda = 10$, and (c) $\lambda = 50$. Light colors for instantaneous values and dark colors for time average value. Note, statistics are collected in a time duration when a wide inertial range is established, and the shaded area is equivalent to the mentioned inertial spectral range in Fig. 2.

Fig. 2(d)]. For $\lambda = 10$, we find $n(A) \sim A^{-0.85\pm0.1}$ [see Fig. 5(b)], leading to an estimated spectrum of $\mathcal{E}(k) \sim k^{-5.3}$ [see Fig. 2(e)]. In the case of $\lambda = 50(\gg k_0)$, $n(A) \sim N_v A^{-0.6\pm0.05}$ [see Fig. 5(c)], resulting in $\mathcal{E}(k) \sim k^{-5.8}$, which again corresponds to our numerical observations [see Fig. 2(f)]. The essence of our vortex population theory is clear: understanding $n(A)$ empowers us to derive the inertial range energy spectra and potential enstrophy spectra for any chosen λ.

While the statistical properties presented shed light on the evolution of vortex count, their sizes, and area distributions, they fall short of explaining the intricate vortex interactions leading to these patterns. These interactions can be nonlocal, facilitating the transfer of energy and enstrophy from the vortex population to distant small-scale filaments. By mapping the network structure of these flow fields, we unlock essential physical insights about their interactions, which we explore in the following section.

IV. NETWORK-THEORY-BASED CHARACTERIZATION OF VORTEX INTERACTIONS

Network analysis presented here extends the information from classical statistics and offers a deeper understanding of vortex interactions concealed in a QG turbulence data. Briefly, we introduce some of the terminologies like nodes, links, weights, and metrics associated with networks, and then proceed to show the interactions and the energy spectra. More information on networks can be found in Refs. [44,45].

A. Networks: Definition and metrics

A weighted network is a mathematical framework consisting of $\mathcal{N}$ nodes, representing the quantities of interest in a system connected by links that represent their interactions and links having associated weights that measure the strength of the interaction. A network can be compactly described by a square matrix of size $\mathcal{N} \times \mathcal{N}$, known as an adjacency matrix, whose elements w_{ij} are the weight of the link from node i to node j. The spectral properties of the adjacency matrix and its associated measures provide insights into the nature of the interactions within the network. In a turbulent flow, important interactions occur between the vortices so that one can construct a mathematical network by using the local vorticity data (at every mesh point in the computational domain) and estimating a kind of induced velocity field throughout the domain. The flow field is divided into Cartesian cells, and the nodes are taken as vortical elements in Cartesian cells, and links represent vortical interactions between them with weights as induced velocities from one vortical element to others. If the flow field is discretized by n_x points in the horizontal direction and n_y points in the vertical direction, the resulting network will have $\mathcal{N} = n_x n_y$ nodes. It is believed that the inertial range of scales is inviscid for high Re [32] so that one can treat each of the vorticity data in some way as a local pointlike vortex and estimate the resulting local velocity field because of all other pointlike vortices. The mentioned approach is used to analyze the turbulent dynamics in various complex dynamical systems, see Refs. [44,46–48]. The velocity induced at a node i because of node j can be modeled by the Biot-Savart law as

$$u_{i\to j} = \frac{|\lambda q(\boldsymbol{x}_i)\Delta x \Delta y K_1(\lambda|\boldsymbol{x}_i - \boldsymbol{x}_j|)|}{2\pi}, \tag{2}$$

where K_1 is the first-order modified Bessel function of the second kind, $\Delta x = \Delta y$ is the cell spacing, and $\boldsymbol{x}_i$ and $\boldsymbol{x}_j$ are the position vectors of i and j nodes, respectively. For a special case of $\lambda = 0$, we have $u_{i\to j} = |q(\boldsymbol{x}_i)\Delta x \Delta y|/[2\pi|\boldsymbol{x}_i - \boldsymbol{x}_j|]$, which is similar to Ref. [44]. In such cases, the adjacency matrix is constructed from the induced velocities $u_{i\to j}$ and $u_{j\to i}$ as

$$w_{ij} = \begin{cases} \phi u_{i\to j} + (1-\phi)u_{j\to i} & \text{if } i \neq j, \\ 0 & \text{otherwise.} \end{cases} \tag{3}$$

The parameter ϕ plays a crucial role, ranging from 0 to 1. At $\phi = 0$, we define $w_{ij} = u_{j\to i}$ (velocity induced at node j because of node i), while at $\phi = 1$, we set $w_{ij} = u_{i\to j}$ (velocity induced at node i because of node j). In both scenarios we deal with a directed network with an asymmetric adjacency matrix. When $\phi = 0.5$, this leads to $w_{ij} = \frac{1}{2}(u_{i\to j} + u_{j\to i})$, establishing an undirected network

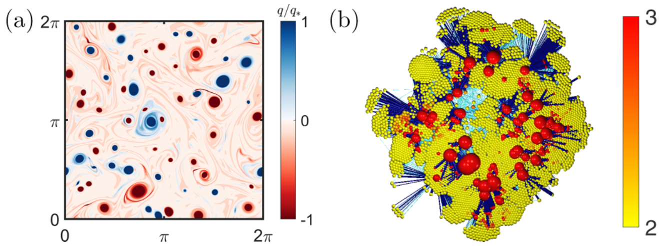

FIG. 6. (a) Potential vorticity and (b) corresponding network structure. Simulations for $\lambda = 0$ and snapshot at $t = 1000\tau_0$. The network is constructed from 4096 nodes (low-pass filtered) information of 2048 × 2048 DNS simulation. Vortical interactions in terms of links (lines) and nodes (circles). Darker and thicker links correspond to larger weights. Links with absolute weight less than ≈2% of the maximum weight are removed for better visualization. Dark red circles are hub nodes, yellow circles are secondary nodes, and the size of the node represents the degree (number of links connected to the node after thresholding). The network is constructed using Graphia [68] as an optimum layout.

with a symmetric adjacency matrix. Notably, asymmetric adjacency matrices yield network spectra that include complex eigenvalues. Recent research [69] scrutinizes the impact of directionality and asymmetry in adjacency matrices on network spectra, revealing that the random addition of directionality to an undirected network preserves the spectrum in a perturbative regime. This means that the nature of interactions revealed by symmetric and asymmetric adjacency matrices coincides greatly. Historically, researchers overlooked link directions, opting for symmetric adjacency matrices, which produced real eigenvalues while estimating various network measures [70]. Computationally, tools to study symmetric matrices are not completely analogous to the asymmetric ones [71]; hence, we use $\phi = 0.5$ to construct symmetric matrices to unmask the interactions (see Supplemental Material [52] for more discussion).

As network metrics [45], both the strength (s) and its distribution, and the length ($\mathcal{L}$) have important roles. The strength at a node i is computed as a sum of weights $s_i = \sum_j w_{ij}$. Nodes with higher strength exhibit greater involvement in dynamics, often identified as hub nodes, showing strengths that can be twice the root mean square value. Disturbances to these hub nodes—such as adding or removing noise—can significantly alter system dynamics. In contrast, nodes that differ from the hubs are generally less influential, suggesting future low-dimensional models [72,73].

In turbulent flow contexts, these hub nodes may manifest as a wide spatial distribution of vortices (with significant size variation) and as uneven clusters of filamentary structures. Rather than relying on traditional methods that utilize the velocity gradient tensor, this network-based approach directly captures information from the vorticity field (easily obtained via stream function-vorticity or velocity-vorticity or three-dimensional simulations) or from velocity field (in experimental setups), allowing for computationally inexpensive analysis. This method significantly simplifies the operations required, minimizing the need for complex higher-rank tensor operations such as eigenvalue extraction or advanced decomposition techniques.

Figure 6 represents an instantaneous vorticity field alongside its corresponding network structure, depicted through nodes, links, and strengths. However, while this colorful depiction of vortices may appear captivating, their influence on turbulent evolution is not straightforward to discern. Furthermore, evaluating the impact of one vortex on another requires consideration of both spatial and temporal dynamics. Additionally, it is misleading to explain the energy transfer mechanism by merely relying on colorful visualizations, like large vortices influencing the dynamics but not the small ones, which is often concluded in the wrong way. The potential ambiguity here is evident in distinguishing between short- and long-range interactions. For instance, does the energy transfer observed in a specific spatial field rely solely on neighboring vortices (through their merging and breaking) or is it also influenced by distant vortices, even with many others interspersed?

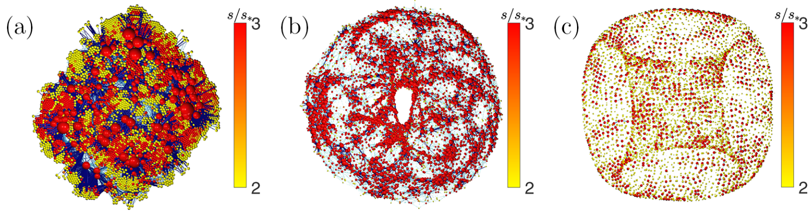

FIG. 7. Turbulent networks of potential vorticity for fields mentioned in Figs. 2(a)–2(c) for (a) $\lambda = 0$, (b) $\lambda = 10$, and (c) $\lambda = 50$. The network is constructed from 4096 nodes (low-pass filtered) of information of 2048×2048 DNS simulation. Darker and thicker links correspond to larger weights. Links with absolute weight less than $\approx 2\%$ of the maximum weight are removed for better visualization. Vortical interactions regarding links (lines) and nodes (circles), whose color represents strength. Dark red circles are hub nodes, yellow circles are secondary nodes, and the network is constructed using Graphia [68] as an optimum layout.

In such scenarios, the network length ($\mathcal{L}$) proves invaluable, revealing the dynamics of node interactions across varied ranges. Typically, the Floyd–Warshall algorithm [74] is employed for computing this length measure, expressed mathematically as

$$\mathcal{L} = \frac{1}{\mathcal{N}(\mathcal{N}-1)} \sum_{i \neq j} \left[\frac{1}{w_{ik_1}} + \frac{1}{w_{k_1 k_2}} + \cdots + \frac{1}{w_{k_m j}} \right],$$

where a shortest network path between nodes i and j traverses all intermediate nodes k_1 to k_m. In a turbulent network, $\mathcal{L}$ can be considered as the average of the minimal advection (commute) time per unit length between every pair of fluid elements [44]. It is evident from Fig. 6(b) that only a limited number of hub nodes (exhibiting strength exceeding twice the rms value) exert a powerful influence across the network domain. Importantly, directly mapping these hub nodes to physical space vortices could be misleading, as the physical environment may also be shaped by the influence of elongated filamentary structures or localized vorticity fields. In the following sections, we will demonstrate the existence of scale invariance among node strengths and leverage this understanding to discern the nature of interactions based on strength distribution.

B. Spatial interactions between vortices via networks

In Fig. 7 we present network structures for various λ values constructed from localized vorticity data. Notably, to build these networks, a complete 2048×2048 mesh is not essential; even a modest grid, such as 64×64, is sufficient. A striking observation is that the network topology highly depends on λ. For $\lambda = 0$, hub nodes are characterized by significant strength, connected by thick links that illustrate nonlocal interactions. In contrast, as λ increases beyond 30, the hub concept becomes less pronounced, resulting in numerous nodes connected by thinner links, showcasing short-range interactions. To delve deeper into the network topology, we computed the normalized probability density of strength, $P(s/s^*)$, at various time instances, as shown in Fig. 8. The color coding in the figure signifies the respective strength of nodes. Weak nodes show a strength often less than $0.5s^*$, while strong nodes show $s > 2s^*$. For $\lambda = 0$ [see Fig. 8(a)], between these extremes, nodes follow a power-law-like strength distribution, $s^{-\gamma}$. At initial time ($t < 100\tau_0$), the scaling exponent $\gamma \approx 2.8 \pm 0.05$, and as time advances, the strength distribution evolves into two power laws with exponents $\gamma_1 \approx 4.2 \pm 0.1$ for $s \ll s^*$ and $\gamma_2 \approx 1.4 \pm 0.1$ for $s \gg s^*$, agreeing with the results of Ref. [44]. This shift in scaling exponent effectively captures the dynamics involved in vortex interactions, forming coherent vortices and filamentary structures as the system evolves from a random initial state. Larger coherent vortices emerge when same-sign vortices unite, influencing long-range dynamics, albeit generating fewer structures. Due to these vortices, a large number of stable filamentary structures are generated during vortex interactions. Over extensive durations,

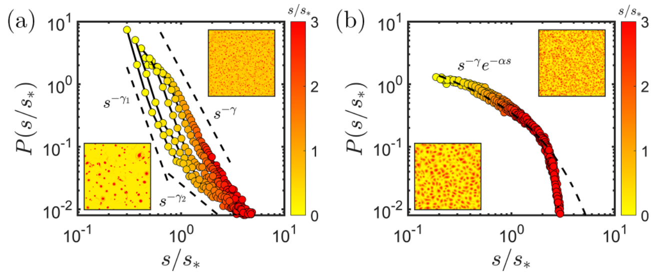

FIG. 8. Network strength distribution $P(s/s*)$ at different instances in time for (a) $\lambda = 0$ and (b) $\lambda = 50$. In panel (a) the distribution evolves from a single power law to a double power law with time (in the form $s^{-\gamma}$); see dashed lines. In panel (b) the distribution shows a universal nature as a truncated power law (in the form $s^{-\gamma}e^{-\alpha\gamma}$). Two insets in each panel for starting (top right) and final time (bottom left) in the inertial range. Lines with symbols for strength distribution at $t = 50\tau_0$, $100\tau_0$, $200\tau_0$, $400\tau_0$, and $600\tau_0$. The colorbar is for strength.

the system exhibits both coherent vortices and filamentary structures that significantly influence the evolving dynamics, giving rise to two power laws γ_1 and γ_2, respectively. From a network perspective, these two power-law behaviors indicate (1) the emergence of new nodes connecting to existing ones and (2) the addition of existing nodes into more dominant structures having larger strengths (coherent vortices).

As λ increases [$\lambda = 50$ shown in Fig. 8(b)], the strength distribution reveals a self-similar nature over time, represented by the form $s^{-\gamma}e^{-\alpha s}$, where $\gamma \approx 0.5 \pm 0.05$ and $\alpha \approx 0.62 \pm 0.05$, which is markedly different from $\lambda = 0$ results. Notably, the strength distribution at $\lambda = 0$ takes on a concave shape with a sharp transition, while for $\lambda > 30$, it shows a convex shape. Furthermore, unlike the two power laws observed over time for $\lambda = 0$, the strength distribution at different time frames for $\lambda > 30$ aligns elegantly with one another, indicating the possible absence of stable filamentary structures. The observed transformation in the strength distribution at high λ indicates that quasifrozen vortices and their interactions maintain self-similarity for a long time. Additionally, the dependence of the Biot-Savart law on the Bessel function for large λ generates flow structures of the order $\mathcal{O}(\lambda^{-1})$, emphasizing the significance of local interactions driving energy transfer in contrast to the nonlocal interactions found in pure 2D turbulence.

Scale-free networks, such as those characterized by power-law distributions, exhibit a remarkable resilience to random disturbances. However, they are particularly vulnerable to changes in dynamics when their hub nodes are disrupted. To evaluate the resilience of turbulence networks against both random and hub-targeted perturbations, we deliberately removed a fraction ($\mathcal{F}$) of nodes—either selected randomly or specifically targeting hubs—and assessed the resulting fractional change in network length, $\delta\mathcal{L} \equiv (\mathcal{L}_{\mathcal{F}}/\mathcal{L}) - 1$. Here, $\mathcal{L}$ represents the original network length with all nodes included, while $\mathcal{L}_{\mathcal{F}}$ reflects the network length postremoval of nodes. The system remains stable or shows similar dynamics if $\delta\mathcal{L} = 0$, but dynamics change if $\delta\mathcal{L} > 0$, making $\delta\mathcal{L}$ a crucial metric for elucidating complex interactions.

In Fig. 9(a), we present both $\mathcal{L}$ (shown in the inset) and $\delta\mathcal{L}$ (shown in the main figure) for different λ values. The network length remains stable over a long duration (more than $600\tau_0$). The network length is small for 2D turbulence compared to that in QG turbulence. Pure 2D turbulence fosters nonlocal interactions with rapid responses between vortices and filaments, unlike QG turbulence, which primarily exhibits local interactions with slow dynamics. Notably, shorter network lengths imply that dynamics in one area can significantly influence distant locations. During our postprocessing analysis at a moment when diverse vortices and filamentary structures coexist (for instance, at time $100\tau_0$), we removed a specified fraction of nodes: (1) randomly (as indicated by circles), and (2) exclusively hubs (indicated with squares). In both pure 2D and QG turbulence, the removal of random nodes (even as large as 10%) had minimal impact on network length,

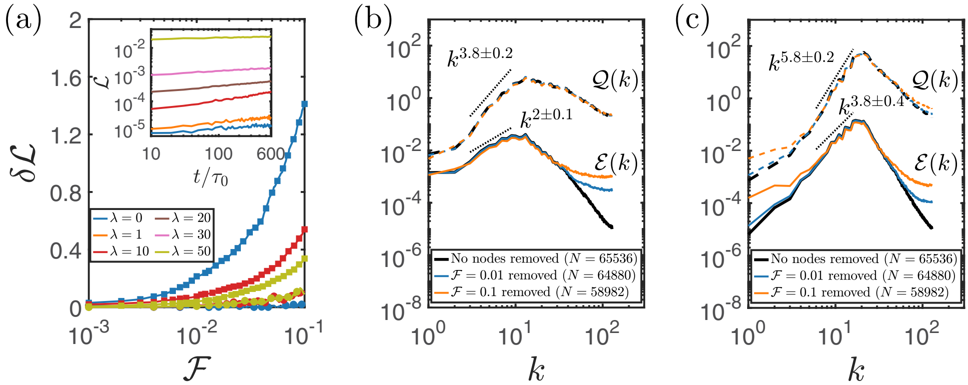

FIG. 9. (a) Resilience of turbulence network against fraction node $\mathcal{F}$ removal for different λ values. Change in network length ($\delta\mathcal{L}$) when a fraction $\mathcal{F}$ of random nodes (circle) and hub (square) nodes are removed. Inset for network length ($\mathcal{L}$) vs time. Spectra reconstruction by removing fraction of nonhub nodes for (b) $\lambda = 0$ and (c) $\lambda = 50$. Note, continuous lines for $\mathcal{E}(k)$ and dashed lines for $\mathcal{Q}(k)$. Information on both small and inertial range wave numbers remains intact to a great extent after removing a fraction of nodes.

maintaining $\delta\mathcal{L} < 0.1$. Yet, when hub nodes were removed, we observed a pronounced alteration in network length, especially within pure 2D turbulence. The pivotal insight gained from analyzing $\delta\mathcal{L}$ is that hubs, including coherent vortices and filamentary structures, are essential to driving pure 2D turbulence. Conversely, the constraints are considerably relaxed in QG turbulence, which relies more heavily on local interactions.

Is high-resolution data truly essential for understanding energy spectra? This work compellingly demonstrates that even low-resolution data—specifically, 256×256 (low-pass filtered) data—can effectively reconstruct energy spectra, negating the need for the more resource-intensive 2048×2048 original resolution. Our findings further reveal that spectral scalings are accurately reproduced, not only within the inertial range but also at small wave numbers, a regime typically requiring extensive statistical data. To investigate, we resampled low-pass filtered data from the original computational mesh and constructed energy spectra for both pure 2D turbulence and QG turbulence. The observed energy spectra (ε) at small wave numbers follow the form k^2 for $\lambda = 0$ and k^4 for $\lambda = 50$, as shown in Figs. 9(b) and 9(c), respectively. Remarkably, when we removed various fractions of nonhub nodes, the integrity of the low-wave-number spectra remained unscathed. The inertial range spectra also persisted without alteration, although the range was slightly narrowed. Analytically capturing energy spectra for large-scale structures, or low wave numbers, presents formidable challenges since traditional concepts like self-similarity do not hold. Our proposed vortex population theory, aimed at the inertial range, exemplifies the necessity of shifting towards network-based analyses, which offer a more robust framework than classical statistical theories.

As a future scope, there is immense potential to explore β-plane turbulence and its complex dynamics through the lens of intricate networks, focusing on the interactions between vortices and mean zonal flows. Additionally, we can pursue the development of low-dimensional models for QG turbulence, leveraging hub nodes while investigating scalar field properties in the context of ramp- and clifflike intermittent structures. The three-dimensional effects, such as the vortex stretching concept, can be reinvestigated. Studies on complex networks open new avenues for scientific inquiry.

V. SUMMARY AND CONCLUSION

We have numerically probed the influence of the inverse Rossby deformation radius (λ) on vortex distribution and interactions within a freely decaying quasi-geostrophic turbulent flow in a double periodic box at moderately high Reynolds number $O(10^4)$. We have extracted vortices from the flow using Rortex criteria, quantifying their number (N_v), mean area (A), and packing fraction, and developed a scaling theory to explain the inertial range energy spectrum as $\mathcal{E}(k) \sim k^{-7+2p}$, where p depends on λ. The found vortex area distributions show self-similar statistics with a functional form $n(A) \sim N_v A^{-p}$. To unmask the insights on short- and long-range interactions between the vortices, we developed time-varying turbulence networks with node strength derived from the Biot-Savart law. In the regime where $\lambda \ll k_0$, we observed long-range vortex interactions that led to a scale-free network topology with a strength distribution of $P(s) \sim s^{-\gamma}$, where $\gamma \approx 2.79 \pm 0.07$. In contrast, for $\lambda \gg k_0$, interactions were predominantly local due to the Bessel function dependence, resulting in a truncated scale-free topology defined by $P(s) \sim s^{-\gamma} e^{-\alpha s}$, yielding $\gamma \approx 0.5 \pm 0.05$ and $\alpha \approx 0.62 \pm 0.05$. Notably, both network topologies exhibited resilience against random perturbations while displaying sensitivity to hub node removal. Furthermore, we demonstrated that energy spectrum scaling at low wave numbers can be effectively captured through the network hubs, significantly reducing the necessary degrees of freedom for examining large-scale vortices in quasi-geostrophic turbulence. Importantly, the large-scale energy spectral scaling that is difficult to explain using classical statistical theories can be shown via the information of the hub nodes within the scale-free network. Finally, we highlight that the long-lived oceanic eddies in midlatitudes can result from local interactions, but they are large in number and take place between small vortices.

ACKNOWLEDGMENTS

We would like to posthumously acknowledge Prof. Roddam Narasimha for his invaluable advice and support in the early stages of our research. We thank Prof. Gautam Biswas (IIT Kanpur), Prof. Meheboob Alam (JNCASR), Prof. Rama Govindarajan (ICTS), Prof. Fazle Hussain (Texas Tech), and two anonymous referees for their encouragement and suggestions regarding our work. V.R.K.P. gratefully acknowledges research support from the Prime Minister's Research Fellows (PMRF) Scheme, Government of India. R.L. acknowledges research grants from the Board of Research and Nuclear Sciences (BRNS), the Mathematical Research Impact Centric Support (MATRICS) scheme, the Department of Science and Technology, and the Government of India for their generous help. We sincerely thank Param Shakti for the computing resources developed under the National Super Computing Mission at IIT Kharagpur, India.

[1] M. Koshlyakov and A. Monin, Synoptic eddies in the ocean, Annu. Rev. Earth Planet Sci. **6**, 495 (1978).

[2] D. B. Chelton, M. G. Schlax, and R. M. Samelson, Global observations of nonlinear mesoscale eddies, Prog. Oceanogr. **91**, 167 (2011).

[3] W. R. Holland and P. B. Rhines, An example of eddy-induced ocean circulation, J. Phys. Oceanogr. **10**, 1010 (1980).

[4] X. Zhai, R. J. Greatbatch, and J. Sheng, Diagnosing the role of eddies in driving the circulation of the northwest Atlantic Ocean, Geophys. Res. Lett. **31** (2004).

[5] C. O. Dufour, S. M. Griffies, G. F. de Souza, I. Frenger, A. K. Morrison, J. B. Palter, J. L. Sarmiento, E. D. Galbraith, J. P. Dunne, W. G. Anderson, and R. D. Slater, Role of mesoscale eddies in cross-frontal transport of heat and biogeochemical tracers in the Southern Ocean, J. Phys. Oceanogr. **45**, 3057 (2015).

[6] P. G. Falkowski, D. Ziemann, Z. Kolber, and P. K. Bienfang, Role of eddy pumping in enhancing primary production in the ocean, Nature (London) **352**, 55 (1991).

[7] D. J. McGillicuddy Jr., A. Robinson, D. Siegel, H. Jannasch, R. Johnson, T. Dickey, J. McNeil, A. Michaels, and A. Knap, Influence of mesoscale eddies on new production in the Sargasso Sea, Nature (London) **394**, 263 (1998).

[8] D. J. McGillicuddy, L. A. Anderson, N. R. Bates, T. Bibby, K. O. Buesseler, C. A. Carlson, C. S. Davis, C. Ewart, P. G. Falkowski, S. A. Goldthwait, D. A. Hansell, W. J. Jenkins, R. Johnson, V. K. Kosnyrev,

J. R. Ledwell, Q. P. Li, D. A. Siegel, and D. K. Steinberg, Eddy/wind interactions stimulate extraordinary mid-ocean plankton blooms, Science **316**, 1021 (2007).

[9] R. Farneti, T. L. Delworth, A. J. Rosati, S. M. Griffies, and F. Zeng, The role of mesoscale eddies in the rectification of the Southern Ocean response to climate change, J. Phys. Oceanogr. **40**, 1539 (2010).

[10] K. Bryan, The role of mesoscale eddies in the poleward transport of heat by the oceans: A review, Physica D **98**, 249 (1996).

[11] D. L. Volkov, T. Lee, and L.-L. Fu, Eddy-induced meridional heat transport in the ocean, Geophys. Res. Lett. **35**, 2008GL035490 (2008).

[12] Z. Zhang, Y. Liu, B. Qiu, Y. Luo, W. Cai, Q. Yuan, Y. Liu, H. Zhang, H. Liu, M. Miao, Z. Jinchao, W. Zhao, and J. Tian, Submesoscale inverse energy cascade enhances Southern Ocean eddy heat transport, Nat. Commun. **14**, 1335 (2023).

[13] I. Kamenkovich, Z. Garraffo, R. Pennel, and R. A. Fine, Importance of mesoscale eddies and mean circulation in ventilation of the Southern Ocean, J. Geophys. Res. Oceans **122**, 2724 (2017).

[14] R. Karsten, H. Jones, and J. Marshall, The role of eddy transfer in setting the stratification and transport of a circumpolar current, J. Phys. Oceanogr. **32**, 39 (2002).

[15] D. B. Chelton, R. A. deSzoeke, M. G. Schlax, K. E. Naggar, and N. Siwertz, Geographical variability of the first baroclinic Rossby radius of deformation, J. Phys. Oceanogr. **28**, 433 (1998).

[16] Y. Lin and G. Wang, The effects of eddy size on the sea surface heat flux, Geophys. Res. Lett. **48**, e2021GL095687 (2021).

[17] T. G. Smith, S.-A. Nicholson, F. A. Engelbrecht, N. Chang, N. P. Mongwe, and P. M. S. Monteiro, The heat and carbon characteristics of modeled mesoscale eddies in the South–East Atlantic Ocean, J. Geophys. Res. Oceans **128**, e2023JC020337 (2023).

[18] W.-J. von Appen, T. Baumann, M. Janout, N. Koldunov, Y.-D. Lenn, R. Pickart, R. Scott, and Q. Wang, Eddies and the distribution of eddy kinetic energy in the Arctic Ocean, Oceanography **35**, 42 (2022).

[19] G. Sutyrin and T. Radko, Why the most long-lived oceanic vortices are found in the subtropical westward flows, Ocean Modell. **161**, 101782 (2021).

[20] R. Wang, F. Nan, F. Yu, and B. Wang, Impingement of subsurface anticyclonic eddies on the Kuroshio mainstream east of Taiwan, J. Geophys. Res. Oceans **127**, e2022JC018950 (2022).

[21] A. J. White and N. R. McDonald, Modelling and predicting the motion of ocean eddies from local current data, Ocean Modell. **13**, 292 (2006).

[22] B. A. Storer, M. Buzzicotti, H. Khatri, S. M. Griffies, and H. Aluie, Global energy spectrum of the general oceanic circulation, Nat. Commun. **13**, 5314 (2022).

[23] Z.-F. Wang, L. Sun, Q.-Y. Li, and H. Cheng, Two typical merging events of oceanic mesoscale anticyclonic eddies, Ocean Sci. **15**, 1545 (2019).

[24] R. Salmon, *Lectures on Geophysical Fluid Dynamics* (Oxford University Press, New York, 1998).

[25] A. J. G. Nurser and S. Bacon, The Rossby radius in the Arctic Ocean, Ocean Sci. **10**, 967 (2014).

[26] G. Boffetta and R. E. Ecke, Two-dimensional turbulence, Annu. Rev. Fluid Mech. **44**, 427 (2012).

[27] P. B. Rhines, Waves and turbulence on a beta-plane, J. Fluid Mech. **69**, 417 (1975).

[28] J. C. Mcwilliams, The emergence of isolated coherent vortices in turbulent flow, J. Fluid Mech. **146**, 21 (1984).

[29] J. C. McWilliams, The vortices of two-dimensional turbulence, J. Fluid Mech. **219**, 361 (1990).

[30] G. F. Carnevale, J. C. McWilliams, Y. Pomeau, J. B. Weiss, and W. R. Young, Evolution of vortex statistics in two-dimensional turbulence, Phys. Rev. Lett. **66**, 2735 (1991).

[31] N. K. R. Kevlahan and M. Farge, Vorticity filaments in two-dimensional turbulence: Creation, stability and effect, J. Fluid Mech. **346**, 49 (1997).

[32] P. Davidson, *Turbulence: An Introduction for Scientists and Engineers* (Oxford University Press, Oxford, 2015).

[33] L. M. Smith and V. Yakhot, Onset of intermittency in two-dimensional decaying turbulence, Phys. Rev. E **55**, 5458 (1997).

[34] S. Kida, M. Yamada, and K. Ohkitani, The energy spectrum in the universal range of two-dimensional turbulence, Fluid Dyn. Res. **4**, 271 (1988).

[35] B. H. Burgess, D. G. Dritschel, and R. K. Scott, Vortex scaling ranges in two-dimensional turbulence, Phys. Fluids **29**, 111104 (2017).
[36] R. H. Kraichnan, Inertial ranges in two-dimensional turbulence, Phys. Fluids **10**, 1417 (1967).
[37] G. K. Batchelor, Computation of the energy spectrum in homogeneous two-dimensional turbulence, Phys. Fluids **12**, II-233 (1969).
[38] P. A. Davidson, On the large-scale structure of homogeneous two-dimensional turbulence, J. Fluid Mech. **580**, 431 (2007).
[39] B. H. Burgess and D. G. Dritschel, Long frontal waves and dynamic scaling in freely evolving equivalent barotropic flow, J. Fluid Mech. **866**, R3 (2019).
[40] B. Burgess and D. Dritschel, Potential vorticity fronts and the late-time evolution of large-scale quasi-geostrophic flows, J. Fluid Mech. **939**, A40 (2022).
[41] V. D. Larichev and J. C. McWilliams, Weakly decaying turbulence in an equivalent-barotropic fluid, Phys. Fluids **3**, 938 (1991).
[42] Z. Gao and N. Jin, Flow-pattern identification and nonlinear dynamics of gas-liquid two-phase flow in complex networks, Phys. Rev. E **79**, 066303 (2009).
[43] M. Murugesan and R. I. Sujith, Combustion noise is scale-free: Transition from scale-free to order at the onset of thermoacoustic instability, J. Fluid Mech. **772**, 225 (2015).
[44] K. Taira, A. G. Nair, and S. L. Brunton, Network structure of two-dimensional decaying isotropic turbulence, J. Fluid Mech. **795**, R2 (2016).
[45] M. E. J. Newman, *Networks* (Oxford University Press, Oxford, 2018).
[46] V. R. Unni, A. Krishnan, R. Manikandan, N. B. George, R. I. Sujith, N. Marwan, and J. Kurths, On the emergence of critical regions at the onset of thermoacoustic instability in a turbulent combustor, Chaos **28**, 063125 (2018).
[47] G. Iacobello, S. Scarsoglio, and L. Ridolfi, Visibility graph analysis of wall turbulence time-series, Phys. Lett. A **382**, 1 (2018).
[48] W. Kobayashi, H. Gotoda, S. Kandani, Y. Ohmichi, and S. Matsuyama, Spatiotemporal dynamics of turbulent coaxial jet analyzed by symbolic information-theory quantifiers and complex-network approach, Chaos **29**, 123110 (2019).
[49] I. Voitalov, P. van der Hoorn, R. van der Hofstad, and D. Krioukov, Scale-free networks well done, Phys. Rev. Res. **1**, 033034 (2019).
[50] A.-L. Barabási and R. Albert, Emergence of scaling in random networks, Science **286**, 509 (1999).
[51] N. Constantinou, G. Wagner, L. Siegelman, B. Pearson, and A. Palóczy, Geophysicalflows.jl: Solvers for geophysical fluid dynamics problems in periodic domains on CPUs & GPUs, J. Open Source Softw. **6**, 3053 (2021).
[52] See Supplemental Material at http://link.aps.org/supplemental/10.1103/PhysRevFluids.10.054402 for details on grid independence study, validation studies of this work, and animations A1, A2, and A3. Additionally, details on the vortex identification procedure and network formulation used in the main text are also provided.
[53] T. Iwayama, T. G. Shepherd, and T. Watanabe, An ‘ideal’ form of decaying two-dimensional turbulence, J. Fluid Mech. **456**, 183 (2002).
[54] A. G. Nair, J. Hanna, and M. Aureli, Selective energy and enstrophy modification of two-dimensional decaying turbulence, J. Fluid Mech. **956**, A12 (2023).
[55] A. Svirsky, C. Herbert, and A. Frishman, Statistics of inhomogeneous turbulence in large-scale quasi-geostrophic dynamics, Phys. Rev. E **108**, 065102 (2023).
[56] A. Bracco, J. C. McWilliams, G. Murante, A. Provenzale, and J. B. Weiss, Revisiting freely decaying two-dimensional turbulence at millennial resolution, Phys. Fluids **12**, 2931 (2000).
[57] J. H. LaCasce, The vortex merger rate in freely decaying, two-dimensional turbulence, Phys. Fluids **20**, 085102 (2008).
[58] G. Haller, An objective definition of a vortex, J. Fluid Mech. **525**, 1 (2005).
[59] S. K. Robinson, A review of vortex structures and associated coherent motions in turbulent boundary layers, in *Structure of Turbulence and Drag Reduction* (Springer, New York, 1990), pp. 23–50.

[60] J. C. Hunt, A. A. Wray, and P. Moin, Eddies, streams, and convergence zones in turbulent flows, Cent. Turbul. Res. 193 (1988).
[61] J. Jeong and F. Hussain, On the identification of a vortex, J. Fluid Mech. **285**, 69 (1995).
[62] J. Zhou, R. J. Adrian, S. Balachandar, and T. M. Kendall, Mechanisms for generating coherent packets of hairpin vortices in channel flow, J. Fluid Mech. **387**, 353 (1999).
[63] C. Liu, Y. Gao, S. Tian, and X. Dong, Rortex—A new vortex vector definition and vorticity tensor and vector decompositions, Phys. Fluids **30**, 035103 (2018).
[64] X. Jiang, A. Lefauve, S. B. Dalziel, and P. Linden, The evolution of coherent vortical structures in increasingly turbulent stratified shear layers, J. Fluid Mech. **947**, A30 (2022).
[65] W. Yin, S. Tao, K. Nagata, Y. Ito, Y. Sakai, and Y. Zhou, Spatial distribution of coherent structures in a self-similar axisymmetric turbulent wake, Phys. Rev. Fluids **8**, 084603 (2023).
[66] J. B. Weiss and J. C. McWilliams, Temporal scaling behavior of decaying two-dimensional turbulence, Phys. Fluids **5**, 608 (1993).
[67] D. G. Dritschel, R. K. Scott, C. Macaskill, G. A. Gottwald, and C. V. Tran, Unifying scaling theory for vortex dynamics in two-dimensional turbulence, Phys. Rev. Lett. **101**, 094501 (2008).
[68] T. C. Freeman, S. Horsewell, A. Patir, J. Harling-Lee, T. Regan, B. B. Shih, J. Prendergast, D. A. Hume, and T. Angus, Graphia: A platform for the graph-based visualisation and analysis of high dimensional data, PLoS Comput. Biol. **18**, e1010310 (2022).
[69] M. Ochi and T. Kawamoto, Contribution of directedness in graph spectra, Phys. Rev. Res. **4**, 033129 (2022).
[70] M. E. J. Newman, Finding community structure in networks using the eigenvectors of matrices, Phys. Rev. E **74**, 036104 (2006).
[71] F. D. Malliaros and M. Vazirgiannis, Clustering and community detection in directed networks: A survey, Phys. Rep. **533**, 95 (2013).
[72] V. Thibeault, G. St-Onge, L. J. Dubé, and P. Desrosiers, Threefold way to the dimension reduction of dynamics on networks: An application to synchronization, Phys. Rev. Res. **2**, 043215 (2020).
[73] N. Masuda and P. Kundu, Dimension reduction of dynamical systems on networks with leading and non-leading eigenvectors of adjacency matrices, Phys. Rev. Res. **4**, 023257 (2022).
[74] R. W. Floyd, Algorithm 97: Shortest path, Commun. ACM **5**, 345 (1962).